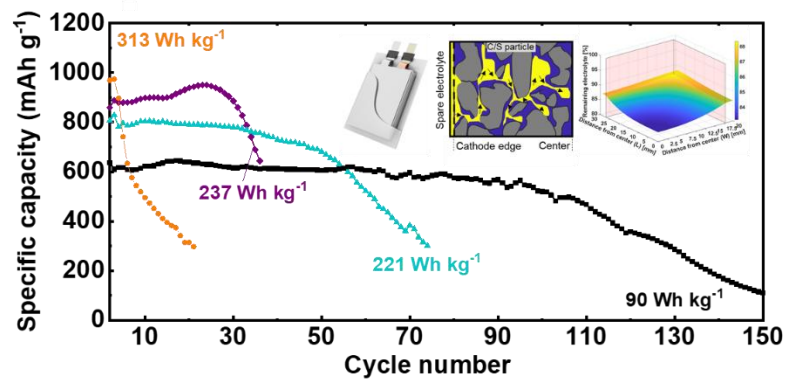




Reaction Heterogeneity in Practical High-Energy Lithium-Sulfur Pouch Cells

Journal:	<i>Energy & Environmental Science</i>
Manuscript ID	EE-ART-07-2020-002088.R1
Article Type:	Paper
Date Submitted by the Author:	21-Aug-2020
Complete List of Authors:	<p>Shi, Lili; Pacific Northwest National Laboratory, Bak, Seong-Min; Brookhaven National Laboratory, Chemistry Division Shadike, Zulipiya; Brookhaven National Laboratory, chemistry division Wang, Chengqi; University of Michigan Niu, Chaojiang; Pacific Northwest National Laboratory Northrup, Paul; Stony Brook University Lee, Hongkyung; Pacific Northwest National Laboratory Baranovskiy, Arthur; Pacific Northwest National Laboratory Anderson, Cassidy; Pacific Northwest National Laboratory Qin, Jian; Pacific Northwest National Laboratory Feng, Shuo; Pacific Northwest National Laboratory Ren, Xiaodi; Pacific Northwest National Laboratory Liu, Dianying; Pacific Northwest National Laboratory Yang, Xiao-Qing; Brookhaven National Lab, Chemistry Gao, Fei; University of Michigan, Michigan, Department of Nuclear Engineering and Radiological Sciences Lu, Dongping; Pacific Northwest National Laboratory, Xiao, Jie; Pacific Northwest National Laboratory, Liu, Jun; Pacific Northwest National Laboratory,</p>



Reaction heterogeneity was discovered as a main reason for Li-S pouch cell degradation at practical high energy.

ARTICLE

Reaction Heterogeneity in Practical High-Energy Lithium-Sulfur Pouch Cells

Received 00th January 20xx,
Accepted 00th January 20xx

DOI: 10.1039/x0xx00000x

Lili Shi,^{‡a} Seong-Min Bak,^{‡b} Zulipiya Shadike,^{‡b} Chengqi Wang,^c Chaojiang Niu,^a Paul Northrup,^d Hongkyung Lee,^a Arthur Y. Baranovskiy,^a Cassidy S. Anderson,^a Jian Qin,^a Shuo Feng,^a Xiaodi Ren,^a Dianying Liu,^a Xiao-Qing Yang,^b Fei Gao,^{c, e} Dongping Lu,^{*a} Jie Xiao,^{*a} and Jun Liu^{*a}

The lithium-sulfur (Li-S) battery is a promising next-generation energy storage technology because of its high theoretical energy and low cost. Extensive research efforts have been made on new materials and advanced characterization techniques for mechanistic studies. However, it is uncertain how discoveries made on the material level apply to realistic batteries due to limited analysis and characterization of real high-energy cells, such as pouch cells. Evaluation of pouch cells (> 1 Ah) (instead of coin cells) that are scalable to practical cells provides a critical understanding of current limitations which enables proposal of strategies and solutions for further performance improvement. Herein, we design and fabricate pouch cells over 300 Wh kg⁻¹, compare the cell parameters required for high-energy pouch cells, and investigate the reaction processes and their correlation to cell cycling behavior and failure mechanisms. Spatially resolved characterization techniques and fluid-flow simulation reveal the impacts of the liquid electrolyte diffusion within the pouch cells. We found that catastrophic failure of high-energy Li-S pouch cell results from uneven sulfur/polysulfide reactions and electrolyte depletion for the first tens of cycles, rather than sulfur dissolution as commonly reported in the literature. The uneven reaction stems from limited electrolyte diffusion through the porous channels into the central part of thick cathodes during cycling, which is amplified both across the sulfur electrodes and within the same electrode plane. A combination of strategies is suggested to increase sulfur utilization, improve nanoarchitectures for electrolyte diffusion and reduce consumption of the electrolytes and additives.

Broader context

As the global energy consumption rises, lithium-sulfur (Li-S) batteries pose as a promising, sustainable energy storage technology. The high theoretical energy and low cost of materials situate Li-S batteries as a realistic advancement beyond Li-ion batteries. Further progression into commercialization is currently held back by the infancy of realistic pouch cell demonstration. This work aims to bring new understanding to cell failure mechanisms, which can then assist in strategic design of cell components and structure and improve cell energy and extend cycle life. To close the gap between the material-level discoveries and the cell-level demonstration, this work shows hindered electrolyte diffusion through the porous electrode is identified as the root cause of reaction heterogeneity at lean electrolyte conditions, which causes the gradual electrode failure propagating from the electrode center to the edge. Utilization of spatially resolved characterization and theoretical simulation on the practical pouch cells with a specific energy >300 Wh kg⁻¹ provides a full spectrum view of the dynamic interactions of key cell components in Li-S batteries.

Introduction

As one of the most promising next-generation battery technologies, the lithium-sulfur (Li-S) battery has been intensively investigated in recent years because of its high energy and low cost.¹ Many roadblocks need to be overcome before large-scale deployment of this new battery technology.² The most well-known problem is the dissolution of polysulfides, which leads to shuttle reactions^{3, 4} and causes the loss of S from the entire cathode. These side reactions greatly affect the electrochemical performance of Li-S cells. Major efforts include employing various carbon hosts,⁵ polymer backbones,⁶ or inorganic oxides^{7, 8} to anchor soluble polysulfides generated during the electrochemical process and improve the cycling

^a Energy and Environmental Directorate, Pacific Northwest National Laboratory, Richland, Washington 99352, United States.

E-mail: dongping.lu@pnnl.gov; jie.xiao@pnnl.gov; jun.liu@pnnl.gov

^b Chemistry Division, Brookhaven National Laboratory, Upton, New York 11973, United States.

^c Department of Nuclear Engineering and Radiological Sciences, University of Michigan, Ann Arbor, Michigan 48109-2104, United States.

^d Department of Geosciences, Stony Brook University, Stony Brook 11794, United States.

^e Department of Materials Science and Engineering, University of Michigan, Ann Arbor, Michigan 48109-2104, United States.

† Footnotes relating to the title and/or authors should appear here.

Electronic Supplementary Information (ESI) available: [details of any supplementary information available should be included here]. See DOI: 10.1039/x0xx00000x

‡ These authors contributed equally to this work.

stability. It was also suggested that with a high S loading, cell failure may be mainly due to Li anode degradation because of the “deep” cycling of Li metal.⁹ Many approaches have been developed to protect the Li metal by adopting additional layers^{10, 11} to eliminate the direct contact between the polysulfide-containing electrolyte and Li, or through the incorporation of additives to alter the solid electrolyte interphase (SEI) properties formed on the Li anode surface to improve the Coulombic efficiency and reduce the shuttle opportunities during cycling.^{12, 13} A wide range of electrolyte additives and polymer electrolytes studies have demonstrated a certain degree of improvement.^{14, 15} However, it has been widely realized now that the progress made at the materials level cannot be easily translated into realistic high-energy cells.¹⁶

Although great efforts have been made to increase cell energy and extend cell cycle life, few reports evaluate the behavior of real high-energy Li-S cells such as pouch cells,^{17, 18} and almost no studies investigate the degradation mechanisms in such cells.^{17, 19} In the literature, a short Li-S cell lifespan is usually attributed to (1) irreversible cathode capacity loss caused by Li polysulfide dissolution²⁰ or electrode passivation,^{21, 22} (2) malfunction of the Li anode as a result of the formation of highly resistive surface layers or Li dendrites,²³ (3) polysulfide crossover-induced shuttle reactions,^{3, 12} or (4) electrolyte consumption.²⁴ In a high-energy cell, the key material parameters, including the amount of cathode (S), anode (Li), and electrolyte, deviate significantly from those normally used in coin cell configurations, thereby leading to very different behaviors, especially cell cycle life.²⁵ It is therefore critical to fabricate realistic high-energy pouch cells and investigate the structure and chemistry of cells over multiple length scales, from nanoscale to electrode level, during cycling in order to identify the dominant reasons for the fast cell degradation.

This paper analyzes important parameters commonly used in coin cells and compares them with those needed for high-energy pouch cells, and then study electrochemical properties of the pouch cells using the desired cell parameters. More importantly, this work provides a careful analysis of the failure mechanisms of Li-S cell at elevated energy levels and sizes using state-of-the-art characterization tools coupled with fluid-flow simulations. The mechanistic study revealed that limited diffusion kinetics causes uneven electrochemical reactions and electrolyte depletions across the electrode as the main causes of cell failure. These results suggest that new materials and strategies are required to produce Li-S cells that have both high specific energies and long cycle lives.

Results and Discussion

1. Limitations of coin cell investigations

Great progress has been made for developing Li-S coin cells that have impressive cycle lives, but only limited cycle lives can be achieved in practical high-energy Li-S pouch cells.^{17, 19} Most Li-S coin cell (<1.6 cm² of electrode size) investigation uses low S loading electrodes (<2 mAh cm⁻²), flooded electrolyte (E/C>42 g (Ah)⁻¹, or E/S>38 mL g⁻¹, where E/C and E/S represent electrolyte volume/capacity and electrolyte volume/S mass, respectively), and an excess amount of Li anode (N/P>25, 250 μm Li, where N/P represents the anode/cathode capacity ratio) (Fig. 1a, b and c). Fig. 1c and f compare the weight distributions of a 2Ah pouch cell using different coin cell and pouch cell parameters. A sulfur utilization rate of 1000 mAh g⁻¹ based on elemental S was used for both cases. Using typical coin cell conditions, i.e., S loading = 2 mg cm⁻², E/S = 38 mL g⁻¹ and 250 μm thick Li, the electrolyte takes >78 wt.% in the whole cell, and the actual cell energy is estimated to be less than 45 Wh kg⁻¹ (Fig. 1a and c, Table S1).

ARTICLE

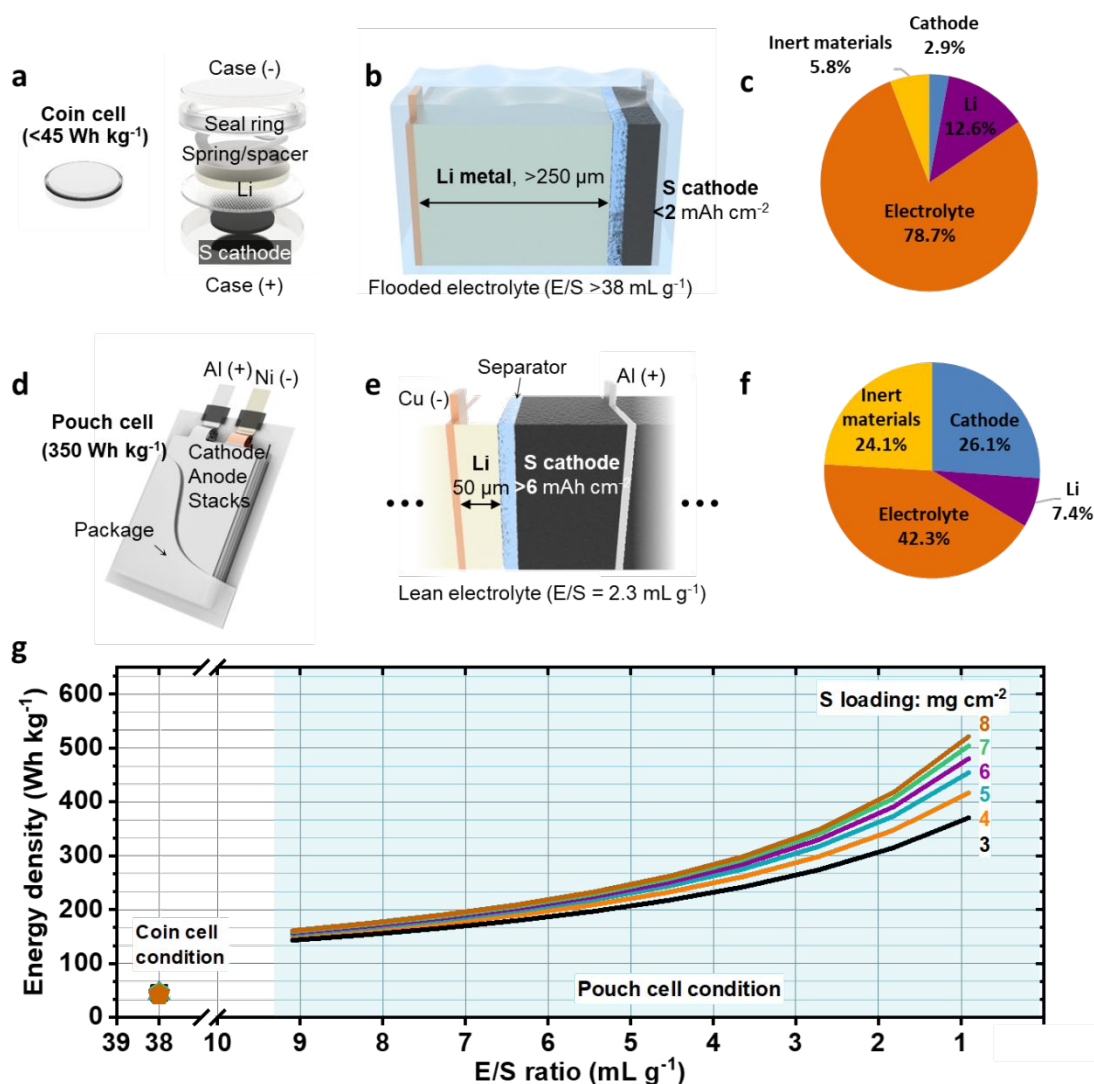


Fig. 1 Comparing coin cells and pouch cells in Li-S study. (a, b) Schematic of a Li-S coin cell using a low loading cathode ($<2 \text{ mAh cm}^{-2}$), flooded electrolyte ($E/S > 38 \text{ mL g}^{-1}$), and excessive amount of Li ($(N/P) > 25$, $250 \mu\text{m}$ Li). (c) Estimation of weight distribution of a Li-S pouch cell using the coin cell parameters. The inert materials include separators, current collectors and tabs, and cell package. (d, e) Schematic of a high-energy Li-S pouch cell with a realistically high-loading cathode, lean electrolyte, and limited amount of Li anode. (f) Estimation of weight distribution of a 350 Wh kg^{-1} pouch cell. (g) Dependence of pouch cell specific energy on S loading and E/S ratio with Li thickness = $50 \mu\text{m}$.

For a pouch cell, the amounts of electrolyte and Li need to be strictly controlled at $E/S = 2.3 \text{ mL g}^{-1}$ and $50 \mu\text{m}$, respectively, to reach a high specific energy of 350 Wh kg^{-1} (Fig. 1d and e). Reducing the electrolyte content while increasing the active S amount are the two minimum requirements for a substantial cell-level energy improvement (Fig. 1f). A steady increase in cell energy with increasing cathode areal capacity is only feasible under tightly controlled electrolyte amount and other inert

weights. Fig. 1g depicts the dependence of cell energy on both S mass loading and the E/S ratio by including all of the cell components in a pouch cell configuration for 2 Ah pouch cells. For example, at a low E/S ratio of 3 mL g^{-1} , the estimated cell-level energy is only 253 Wh kg^{-1} if S loading is 3 mg cm^{-2} . This value is improved to 330 Wh kg^{-1} , if S loading is increased to 8 mg cm^{-2} . By contrast, if a coin cell uses a high E/S ratio of 38 mL g^{-1} , even with 8 mg cm^{-2} high sulfur loading and $50 \mu\text{m}$ Li, the

cell-level energy is still below 45 Wh kg^{-1} . The estimation results shown in Fig. 1g also clearly indicate that simply increasing the mass loading of S will not lead to an increase in cell energy unless the electrolyte amount is reduced concurrently, while maintaining S utilization.

Note that the pouch cell results are based on a 2 Ah cell with adjustable thickness, which provides a good platform to gain knowledge of cell failure. The pouch cell can be easily scaled up. It is known that if a large cell dimension is adopted, at the same S loading and E/C ratio, cell energy will be further increased.²⁶

2. Electrochemical Performance of the high-energy Li-S pouch cell

Following the aforementioned pouch cell design, practical pouch cells with different E/S ratios were fabricated and tested. Large-areal S electrode coating (Fig. 2a) was obtained by using the integrated Ketjen Black/S cathode material reported earlier.⁹ Multiple layers of S cathodes, separator, and $50 \mu\text{m}$ Li anodes (Fig. 2b) were alternatively stacked together assembling into 2 Ah pouch cells (Fig. 2c). The cell specific energy mentioned here is based on the whole cell weight including the dry cell, electrolyte, and the package materials (Table S2). At a moderately low E/S ratio of 6 mL g^{-1} , the pouch cell delivered a specific energy of 90 Wh kg^{-1} and can maintain for 108 cycles before the capacity decay (Fig. 2d). At a lower E/S ratio of 4 mL g^{-1} , the specific energy was increased to 221 Wh kg^{-1} and maintained for 53 cycles. When the E/S was reduced to 3 mL g^{-1} , the specific energy was increased to 237 Wh kg^{-1} with a cycle life of 35 cycles. To reach the cell energy above 300 Wh kg^{-1} , the E/S ratio needs to be further reduced. A high cell level energy of 313 Wh kg^{-1} was achieved at E/S 2.5 mL g^{-1} at 0.05 C after a formation cycle at 0.02 C (corresponding 1st discharge capacity 1157 mAh g^{-1}) with two typical discharge plateaus at 2.2 V and 2.0 V and a specific discharge capacity of 970 mAh g^{-1} (Fig. S2). However, the extremely low E/S ratio results in an exacerbated cell degradation, lasting for only 5 cycles before a quick decay.

To investigate the correlations of cell cycling and electrolyte amount, the cumulative specific discharge capacity (the total discharge capacities delivered in the lifespan) were plotted versus both applied E/S ratio and active E/S ratio which is estimated by subtracting the pore-filling E/S ratio (see supporting information) from the applied E/S ratio (Fig. 2e). To be consistent with previous discussion, our discussion is still based on the applied E/S ratio since a fixed pore-filling E/S ratio was used for all the active E/S calculation. In the moderately low E/S ratio range ($3 \sim 10 \text{ mL g}^{-1}$), the cumulative specific discharge capacity decreases almost linearly with the E/S ratio as the green fitting line shows. Slope of the fitting line ($k=15$) means the ratio of the change of cumulative specific capacity to the change of E/S ratio. It indicates that the electrolyte consumption is at a constant rate and is a main reason for the cell degradation. Electrolyte consumption in Li-S cell is driven by complicated factors through multiple pathways. First, chemical reactions. It is well established that no component of the present electrolyte (LiTFSI/DOL/DME+ LiNO_3) is thermodynamically stable against Li metal. The chemical reactions on Li start upon cell assembly. During repeated cycling, the Li anode reacts with the electrolytes and generates more active surface areas, which exaggerates the electrolyte consumption. Chemical reactions between the electrolyte components and polysulfides also exist and contribute to the electrolyte consumption. Second, electrochemical reactions. Upon electro-polarization, some of the electrolyte components may get oxidized or reduced at the energized cathode and Li anode. For example, decomposition and polymerization of DOL,²⁷ decomposition of LiNO_3 ,^{28, 29} and decomposition of LiTFSI on both the cathode and Li anode.¹² More interestingly, when the E/S ratio is further reduced to extremely low level ($<3 \text{ mL g}^{-1}$), the slope (40 vs. 15) becomes much steeper as the orange fitting line shows. This means in the E/S ratio range $<10 \text{ mL g}^{-1}$, there would be different mechanisms accounting for the cell degradation, which will be discussed in the following sessions.

ARTICLE

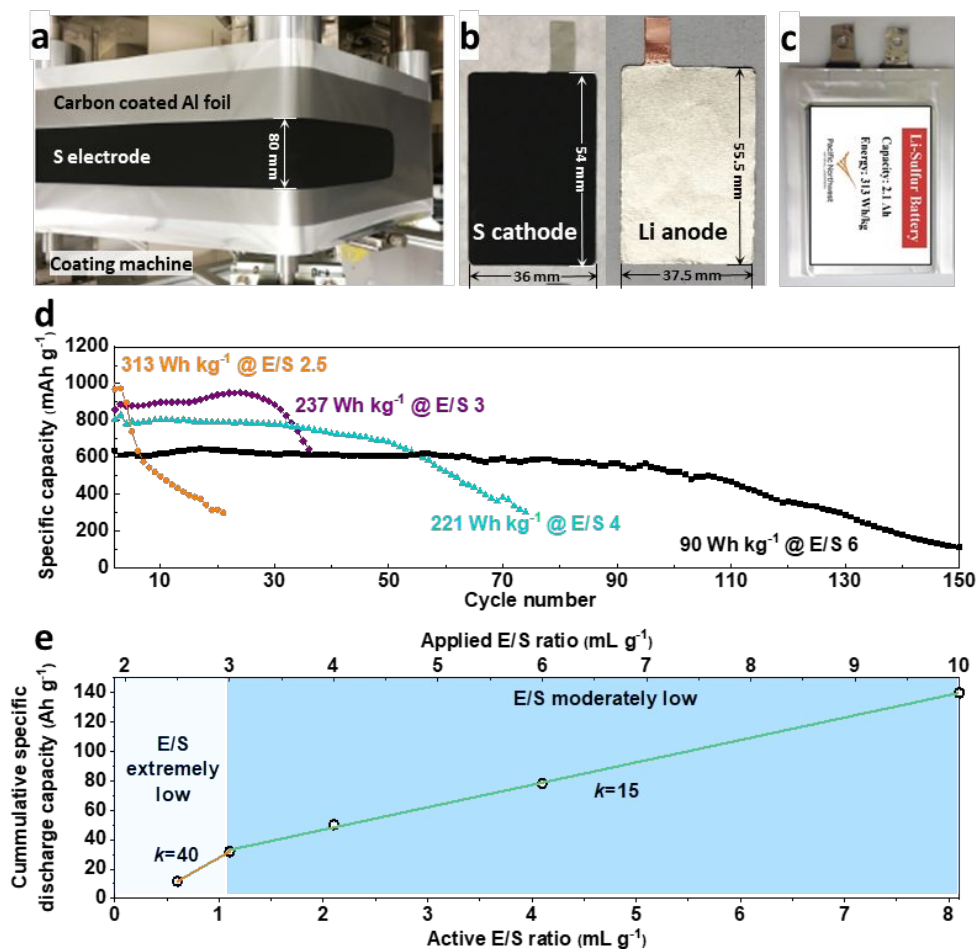


Fig. 2 High-energy Li-S pouch cell. (a) Digital photograph of the large-area S electrode on a coating machine. (b) Digital photographs of punched S cathode and Li anode (thickness = 50 μm) for pouch cell. (c) Digital photograph of the high energy pouch cell. (d) Cycling performances of Li-S pouch cells with different energy densities and E/S ratios (mL g^{-1}). (e) Relationship of the cumulative specific discharge capacity, applied E/S ratio, and active E/S ratio of pouch cells in (d).

3. Failure mechanism of high-energy Li-S pouch cells

To understand the origin of the cell degradation at the extremely low E/S ratio condition, the cycled high energy pouch cell (313 Wh kg^{-1}) was disassembled, and the harvested S cathodes and Li anodes were further analysed to understand the electrochemical and chemical reactions inside the pouch cell. The cycled S cathode was punched into smaller electrodes and reassembled into coin cells coupled with fresh Li and electrolyte. The first discharge capacity of the reassembled Li-S coin cell was very limited at 73 mAh g^{-1} (Fig. S1a). However, a high charge capacity of 1513 mAh g^{-1} was observed for the first charging process, and the subsequent discharge capacity was improved to 1298 mAh g^{-1} . This indicates that the cell after 22

cycles is in a partially discharged state dominated by short chain polysulfides or Li sulfide, which is caused by internal short (Fig. S1c). The high reversible capacities delivered of the reassembled cell verifies that most of the S is deactivated temporarily after pouch cell failure and can be recovered to its original activity after coupled with fresh Li anode and electrolyte. Even when the reassembled cell was tested using a restricted amount of electrolyte and Li anode, more than 1000 mAh g^{-1} capacity was observed (Fig. S1b). These results strongly suggest that for such an early cell failure, most of the S is still active within the cathode matrix, and thus the S dissolution and loss is not a dominant reason for the fast capacity degradation of the high-energy Li-S pouch cell.

Uneven sulfur reactions within cathode layers. The reported S loss, S redistribution and electrode passivation are mostly based on the observations in Li-S coin cell study. In the pouch cell studied here, the electrode has a 15 times larger area and greatly increased areal capacity or S loading. Each layer of the thick S cathode plays an equally important role in delivering capacity/energy. Additionally, the cathode layers and Li anode alternate in a tight stack inside the pouch. These conditions may cause mass transport problem in large size electrode, resulting electrode morphology, chemical composition, and electrochemical reactivity heterogeneities. Accordingly, three different locations on the same cathode layer were selected for further analysis (Fig. 3a): the near-tab region (R1), the center (R2), and the corner region (R3). After cycling, the electrode surface of these three different locations all became smoother compared to their pristine morphologies (Fig. S3a, b, d, and e). This is due to the redistribution and deposition of S species in the cathode (Fig. S3c and f).^{20, 30} Such S species redistribution along with the volume expansion has direct effects on the electrode morphology.³¹ The loaded S dissolves out of the carbon pores generating empty pores, which demand more of the electrolyte for pore-filling at the beginning of the cycling. In addition, the S species redistribution and deposition would increase the electrode tortuosity and even block the electrolyte redistribution.

Reassembled coin cells using the cycled S cathodes punched from R1, R2, and R3 delivered almost identical reversible capacities of 1030 ~ 1076 mAh g⁻¹ (Fig. S4), which are comparable to those of fresh S cathodes (Fig. S2). The maintenance of active S in different regions of the enlarged cathode layer is consistent with the early conclusion that although polysulfide migration happens during cycling, most of the dissolved polysulfide species are trapped within the thick cathode matrix, and polysulfide dissolution out of the cathode is not a significant problem.

Chemical information about the S species regarding the composition and distribution was investigated using combined X-ray fluorescence microscopy (XRF) and S K-edge X-ray absorption spectroscopy (XAS) analysis, which not only provides global elemental distribution information at the electrode level, but also probes the local chemical status of S species at the micron scale.³² Fig. 3 depicts XRF and XAS spectra results from the R1–R3 regions (Fig. 3a) of the cycled S cathode. Fig. 3b shows the XRF image collected at R1 (7×7 mm) below an energy of 2469 eV, which only detects S species that have relatively low absorption energies.^{20, 33} Apparently, this area is covered mainly by high-intensity S species (in yellow color) and randomly distributed low-intensity S species (in blue color). Further XAS analysis reveals that both the yellow and blue spots are composed of low-valence S species from Li polysulfides or Li sulfides. When the scan cut-off energy is increased to 2480 eV (Fig. 3c), more S species with a wider valence range from S²⁻ to S⁴⁺ can be detected.³³⁻³⁵ This confirms that the R1 region is uniformly covered by S species that have a consistent chemical composition. Similar results were observed in the R3 region (Fig. 3h, i, and j). However, more significant differences were found in the center region of the electrode (R2). Compared to R1 and R3, R2 experiences much more serious heterogeneous reactions, as proved by the XRF mapping at both 2469 and 2480 eV (Fig. 3e and f). In addition, more significant chemical composition heterogeneity was detected by XAS. There are higher contents of sulfone (from TFSI) and S⁶⁺ (from SO₄²⁻) in the yellow spots than in the blue spots (Fig. 3g), which may be caused by residual of TFSI⁻ as a result of earlier solvent depletion in R2 or oxidation of the S species by LiNO₃.^{12, 36} Comparison of XRF and XAS results at these three cathode regions indicates that reaction non-uniformity exists over multiple length scales, from micron domains to the entire electrode. Compared to reactions near the tab or the corner (R1 or R3), the center region (R2) has much higher reaction non-uniformity.

ARTICLE

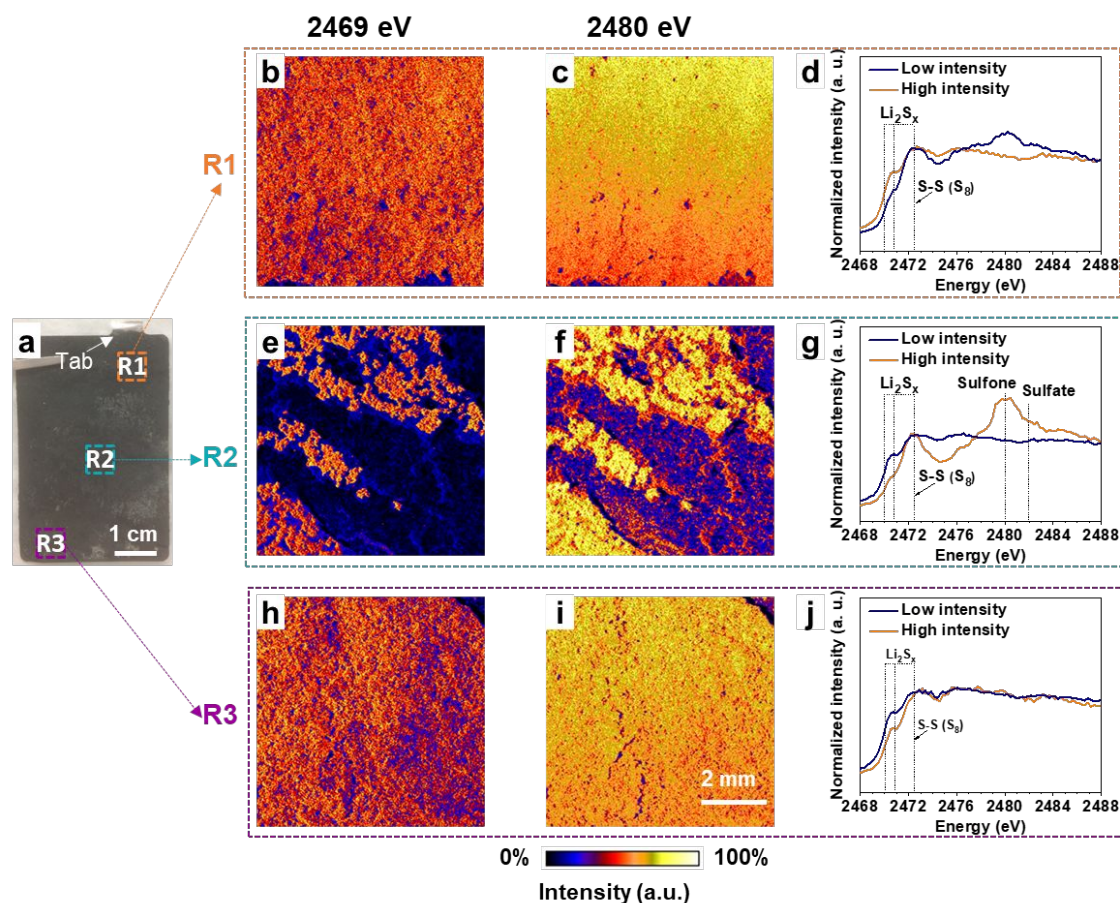


Fig. 3 Revealing the local chemical nature of cycled sulfur cathode by combined XRF and XAS analysis. (a) Digital photograph of the S cathode obtained from the cycled 313 Wh kg^{-1} pouch cell with indicating boxes for three selected spots of interest: outer region nearby electrode-tab (R1), central region (R2), and far corner region (R3). Corresponding mappings of XRF ($7 \text{ mm} \times 7 \text{ mm}$) at two different energy levels (2469 and 2480 eV) to investigate the distribution of S species at the regions of R1 (b and c), R2 (e and f), and R3 (h and i), respectively. XAS spectra (d, g, and j) within an energy scanning range of 2468–2488 eV at two strong contrasted areas in the XRF image (b, f, and h), respectively. The XAS spectrum provides the information about chemical majority in two distinct colored areas: a blue-colored area (corresponding to the blue line in the XAS spectra) in which low-intensity S species are composed of Li sulfide and Li polysulfides; and a yellow-colored area (corresponding to the yellow line in XAS spectra) in which high-intensity S species attributes reflect different compositions—mainly Li sulfide and Li polysulfides in R1 and R3 and more sulfone and sulfate in R2. XRF imaging and XAS spectra clearly indicate uneven S reactions and electrolyte depletion occurred, especially in R2 region.

Inhomogeneous reactions on the same Li anode layer: The morphology and chemical status of the cycled Li anode were also investigated. A significant morphology change in the cycled Li anode was observed. More severe morphological changes were observed near the tab or the far corner of the Li anode (Fig. 4a). A close scanning electron microscope (SEM) observation of the cycled Li anode indicates that the Li anodes in the R1 and R3 regions are very similar and have highly porous structures composed of nanowires, while the R2 region exhibits a relatively denser Li structure with larger average particle size

(Fig. 4b, e, and h), indicating more Li metal residual at electrode centre area. These results are consistent with observations on the S cathode side; i.e., electrochemical reactions are more aggressive at the R1 and R3 locations and are relatively mild in the center region of the electrode. Like in S cathode, the Li pulverization upon repeated plating and stripping alters the electrolyte redistribution. As a result, more electrolyte fills into the newly generated pores in the Li anode and lose the function to support cell cycling. The pore volume expansion of both S cathode and Li anode causes electrolyte redistribution and

worsens the electrode wetting status at the given E/S ratio, which reduces not only S reaction kinetics but also shortens the cell lifespan.

X-ray photoelectron spectroscopy (XPS) was used to study the chemical information of the cycled Li anode in those three regions. Nanoscale composition analysis of the SEI shows that the C1s peak has a very similar overall intensity in R1 and R3 (Fig. 4c and i) but displays a much lower intensity in R2 (Fig. 4f). The binding energies of C1s at 284.6 and 286 eV are assigned to the vibration of C-C and C-O, respectively, which are derived from the electrolyte decomposition products RCH₂CH₂OR' (Li) and RCOOR' (Li) (R and R' are organic groups).^{12, 37-39} The strong

C-C and C-O peaks in the R1 and R3 regions suggest extensive electrolyte side reactions, while the weak and broad peak at R2 reflects less organic electrolyte decomposition products. This also agrees well with the Li1s spectra where more inorganic compounds like LiF and higher Li content were identified in R2 (Fig. 4d, g, j, and Fig. S5). More Li stripping and deposition occur in the R1 and R3 regions and provide more active sites for electrolyte decomposition.⁴⁰ In contrast, the Li anode in the center region has a much lower reaction depth, and probably stops in the participation of the electrochemical reactions already at early stages of cycling as a result of electrolyte shortage.

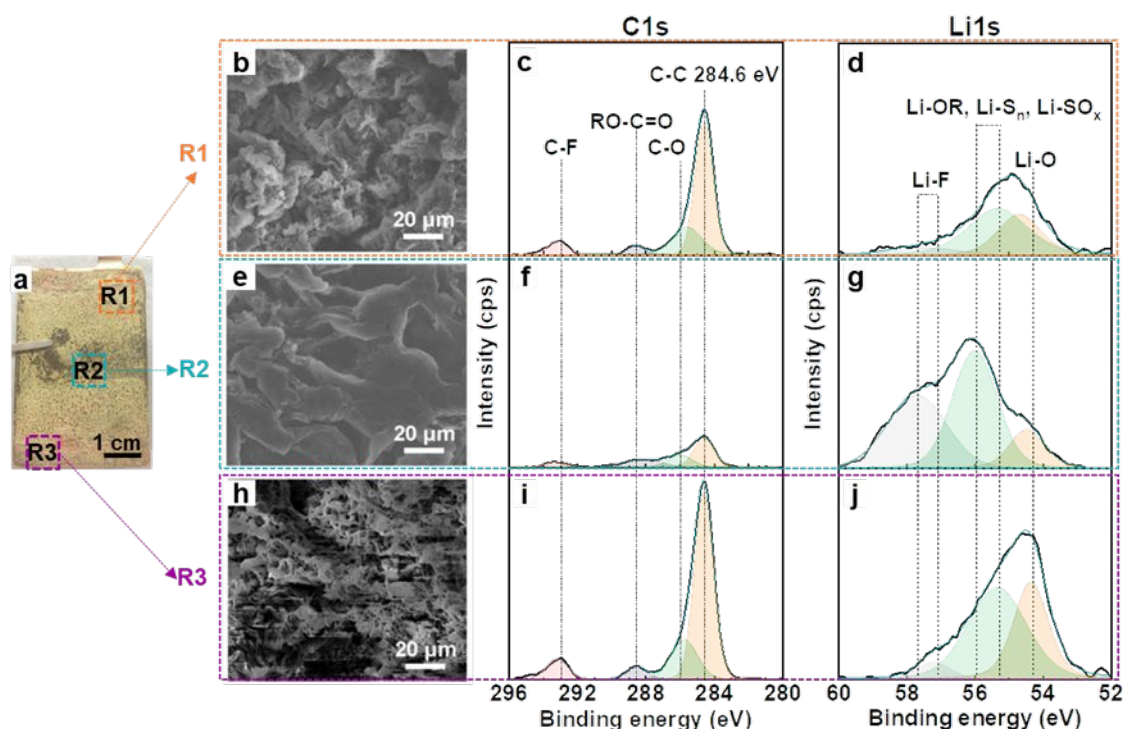


Fig. 4 Morphological and chemical analysis of three different regions of the cycled Li anode. (a) Digital photograph of the Li anode obtained from the cycled 313 Wh kg⁻¹ pouch cell with indicating boxes for three selected spots of interest: outer region near the electrode tab (R1), central region (R2), and far corner region (R3), respectively. Corresponding SEM images (b, e, and h) and high-resolution C1s (c, f, and i) and Li1s (d, g, and j) XPS spectra in R1 (b, c, and d), R2 (e, f, and g), and R3 (h, i, and j).

Limited electrolyte diffusion as the root causes of heterogeneous reactions in Li-S cells: Electrode reaction heterogeneity is identified in Li-S pouch cell and potentially related to the nonuniform electrolyte distribution. To understand the electrolyte distribution along the large-size and porous electrode during cell cycling, a multiphysics simulation coupling Darcy porous flow and species transportation was performed (Fig. 5). For simplicity, one quarter of the cathode area was simulated (Fig. 5a). In the simulation, chemical reaction was assumed to occur at the bottom surface of the anode to deplete the electrolyte. The reaction rate was estimated based on the electrolyte amount and the cycle life of the Li-S pouch cell. The electrolyte transfer process was

modelled by solving the time-dependent diffusion equation for the spare volume. For electrolyte diffusion in the porous cathode and separator, an effective diffusion coefficient considering porosity and tortuosity was adopted (Fig. 5b). After electrolyte injection and upon a long rest period (24 hr), the electrolyte fully wets the nanosized domains of the electrode while the excess portion of electrolyte is stored along the edge area (Fig. 5c). Upon cell cycling, electrolyte depletion starts because of the unavoidable side reactions on both the cathode and Li anode. According to Lewis' theory,^{41, 42} as driven by electrolyte concentration gradient, the electrolyte diffuses through the interconnected pores to replenish the electrolyte loss. However, such diffusion is hindered by the high tortuosity

of the porous electrodes, especially when stacking pressure is applied. Simulation results indicate that the electrolyte content maintains >94% of its original volume and is sufficient to promote the S reaction in the first 50 hours of cycling (Fig. 5d). During the 100–150 hours of cycling (2–3 cycles) (Fig. 5e and f), the electrolyte amount keeps decreasing with a steeper electrolyte concentration gradient. Because of the low current density, the decreasing electrolyte has not yet caused significant cell polarization, as evidenced by the fully overlapped discharging curves (Fig. 2c). However, after 200 hours of cycling, the continuous electrolyte consumption triggers the electrolyte deficiency emerging from the center (Fig. 5g). Half of the electrodes (50.3%) have an electrolyte content less than 85% (Fig. 5h). The electrolyte distribution heterogeneity deteriorates over time and imposes electrochemical polarization on S conversion, and eventually discontinues the electrochemical reactions starting from the

center regions. This is supported by the experimental observation that the exaggerated energy decay was observed starting during the 6th cycle (224 hr, Fig. S6). The electrolyte distribution heterogeneity is attributed to the competition between the electrolyte diffusion across the porous electrode and its consumption. In addition, the simulation predicts that the electrolyte distribution heterogeneity mainly exists in the planar direction. In the perpendicular direction, the electrolyte difference is negligible (Fig. S7) and is due to the shorter electrolyte diffusion distance compared to that along the planar direction.

Consequently, it is crucial to facilitate electrolyte diffusion and redistribution in the large-size and porous electrodes, especially along the planar direction. Simulation indicates that the reaction heterogeneity can be largely reduced by changing the pore geometry and tortuosity (Fig. 5i), which will be discussed in more details below.

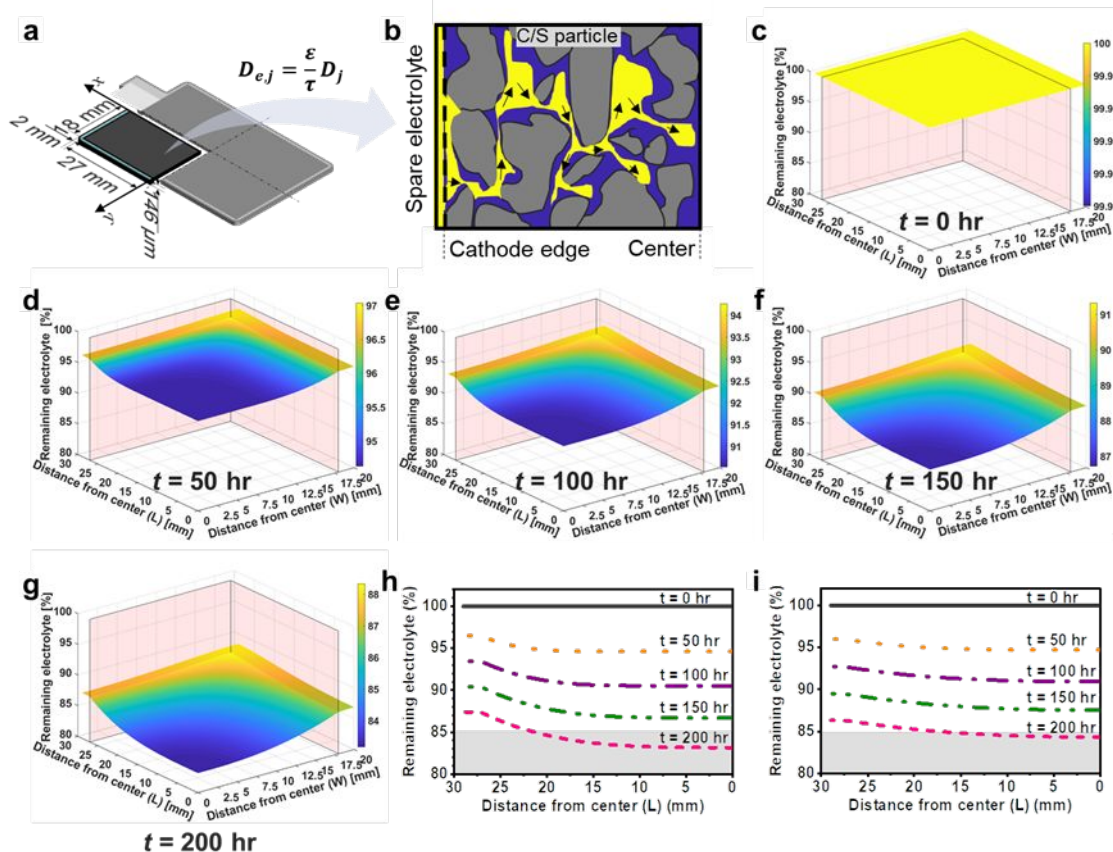


Fig. 5 The multiphysics simulation of the electrolyte diffusion and redistribution in a large-size pouch cell upon cycling. (a) Schematic illustration of the selected electrode dimension (one quarter of the pouch cell) for simulation. (b) Schematic illustration of electrolyte diffusion through nanopores of the cathode. (c, d, e, f, and g) Electrolyte distribution maps at half of the electrode thickness (0.073 mm) after different reaction time. The color from yellow to dark blue corresponds to the electrolyte content (%) filling in the electrode from high to low. Note that the 100% electrolyte content means that all the pores are filled with electrolyte. As long as the content is less than 100%, the electrode may suffer from electrolyte deficiency; i.e., pores are not fully wetted by electrolyte. (c) $t = 0$ hr. (d) $t = 50$ hr. (e) $t = 100$ hr. (f) $t = 150$ hr. (g) $t = 200$ hr. Electrolyte content variation at different times and locations ($x, y = 0$ mm, $z = 0.073$ mm) along the long side of pouch cell: (h) in the currently used S cathode; (i) in the designed S cathode with decreased tortuosity.

ARTICLE

4. Discussion of potential strategies for mitigating the electrolyte deficiency for extended cycle life

It has been recognized that a high-energy Li-S cell is feasible through the simultaneous integration of a high-loading S cathode, a lean amount of electrolyte, and thin Li anode. However, achieving long cycling of high-energy Li-S cells proves very challenging using these cell parameters designed for the high-energy goals. From the present study, it is clear that even when the electrolyte is uniformly distributed across the entire electrode in the beginning, the electrochemical and chemical reactions drive the loss of electrolyte in different regions of the electrodes. While the electrolyte in the marginal area of cathodes may get replenished, it is more difficult to refill the central part of the cathode. If electrolyte diffusion from the edges cannot provide enough electrolyte promptly to the center, electrolyte deficiency will evolve from the central cathode and propagate to the edges, leading to the gradual cathode “shut off” from the center to the edges. To improve cell cycle life at high-level energies, new ideas related to materials, electrode architectures, and electrolytes are needed, particularly with a focus on how to increase electrolyte supply, facilitate electrolyte diffusion, and reduce electrolyte consumption under realistic conditions.

First, S utilization should be improved to increase electrolyte supply. A significantly higher S utilization rate will reduce the requirements for excessive thick electrodes and high S loading. The reduced sulfur will increase the amount of available electrolyte. For example, using 6 mAh cm⁻² S cathode, which is the product of the S mass loading (6.0 mg cm⁻²) with a specific discharge capacity (1000 mAh g⁻¹), the E/S ratio needs to be reduced to 2.4 mL g⁻¹ to achieve a 350 Wh kg⁻¹ cell energy (Fig. 6a). With an improved S utilization rate of 1300 mAh g⁻¹, the S loading can be reduced to 4.6 mg cm⁻² to obtain the same 6 mAh cm⁻² areal capacity. The reduced S mass loading will significantly increase the E/S ratio to 3.9 mL g⁻¹. In addition, the reduced thickness of the S cathode will enhance the electrolyte penetration and redistribution during cycling, enabling extended cell lifespans. Additionally, improving S utilization makes it possible to achieve much higher cell energies over 350 Wh kg⁻¹ without the use of a higher S loading cathode (Fig. 6b). New material designs and functional electrode additives that help to increase the active surface area between S, conductor, and electrolyte,⁴³ accelerate polysulfide conversion,⁴⁴ and promote the formation of small and uniform solid sulfides⁴⁵ will be desired to improve the S utilization rate.

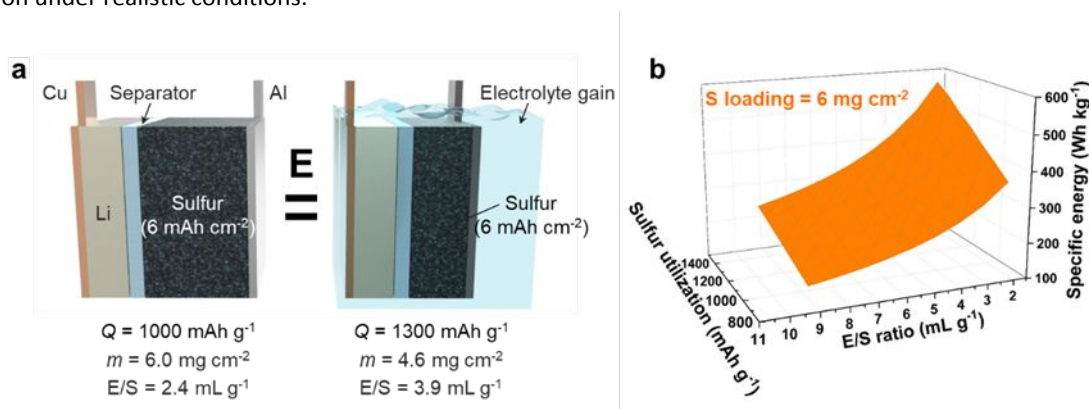


Fig. 6 Strategies for mitigating the electrolyte deficiency for extended cycled life. (a) Schematic illustration of the effect of S utilization rate on the electrode loading and E/S ratio for a 350 Wh kg⁻¹ pouch cell. (b) Dependence of cell specific energy on S utilization and E/S ratio with S cathode loading at 6 mg cm⁻².

Second, the planar electrolyte diffusion rate should be increased. A sufficient planar electrolyte diffusion rate will effectively alleviate the planar heterogeneity in electrolyte distribution and electrochemical reaction, which is supported by the simulation results and is crucial to cell cycle life. A high diffusion rate is dependent on large porosity or low tortuosity of the S cathode and the separator. Because the porosity needs to be minimized to meet the goals of using a lean amount of electrolyte, the tortuosity needs to be particularly reduced. The

simulation results indicate that if the electrode tortuosity can be decreased to a relatively low level, for example, by using aligned pore structures, the electrolyte diffusion through the nanopore channels will be enhanced, and thus the electrolyte heterogeneity problem will be significantly improved (Fig. S8). For a long time, highly porous nanocarbon material has played a significant role in improving cell performance based on the encapsulation reaction mechanism,⁵ but it also introduced high porosity and high tortuosity to S cathodes and separators,

which is contrary to today's high energy density battery demands. A more important question is whether S immobilization in nanopores really works in high S content electrodes (>70 wt.%). If not, can a Li-S cell be made using non-encapsulation approaches?⁴⁶ If these questions can be answered, a low-porosity S cathode/separator with 3-D connected nanopore channels may be developed for future Li-S cells. Therefore, a clear understanding of the impacts that porosity/tortuosity have on reaction kinetics and cell life through combined experimental and simulation approaches is critical for the rational design of a S cathode. Approaches that can reduce the tortuosity^{47, 48} in low-porosity cathodes and separators and maintain sufficient Li⁺ conductivity under lean electrolyte conditions are desired for an improved cell life at high energies.

Third, further efforts should be made to develop stable electrolytes or electrolyte additives. Two factors should be considered. One critical prerequisite for electrolyte selection is the electrolyte's long-term durability when contacting the Li anode in the presence of polysulfides. The other factor is the electrolyte's affinity with the cathode materials for efficient electrode wetting. So far, LiNO₃ is still the most effective additive to protect Li anode from extensive reactions with electrolyte and polysulfide. However, it is consumable and depletes quickly upon chemical and electrochemical reactions.^{28, 49} Design of functional additive molecules/ions that can generate effective SEI on the Li anode in the presence of polysulfides is needed. In the past few years, "non-solvating" electrolytes have been investigated but have not been implemented in high-energy Li-S cells.^{14, 50-52} Recently, concentrated or localized concentrated electrolytes have received widespread attention for prolonging the cycle life of the Li metal anode in NMC-Li cells.^{53, 54} Similar electrolytes or additives have not been developed for Li-S cells without sacrificing the wetting and polysulfide reaction efficiency.⁵⁵ The lessons learned from the Li-NMC systems suggest that a more systematic evaluation of the solvents and additives with polysulfides and Li metal using both computational and experimental techniques will be necessary. More durable and compatible electrolytes or additives may provide the most important opportunity for future Li-S cells. Another option will be the design and development of "solid-state" Li-S cells.^{56, 57} In such cells the Li metal, in principle, is separated from the polysulfides and therefore affords much longer and deeper cycling.^{58, 59} This approach would be attractive only if it can be scaled up without sacrificing the cell-level energy with all components considered.

Experimental

Materials and Methods

Preparation of sulfur (S) cathode. All the chemicals were used as received. The S host material, integrated Ketjen black (IKB), was prepared based on the previously reported approach.⁹ In brief, Ketjenblack (KB, AkzoNobel) and citric acid (Sigma-Aldrich) were firstly mixed in water in a weight ratio of 1:1 and

stirring at 60°C for 2 h. Then ethylene glycol (Sigma-Aldrich) was added into the dispersion at a ratio of ethylene glycol/citric acid = 2:1 mol/mol and stirred at 130°C for 6 h. The mixture was dried overnight and calcined in a tube furnace at 800°C for 10 h at an argon atmosphere. The obtained IKB was ground and sieved with 100 meshes. To prepare the IKB/S composite, S powder (Alfa Aesar) was loaded into the pores of IKB via a melt-impregnation process at 155°C for 12 hours. The S content in the IKB/S composite was 80 wt.%. The IKB/S cathode was prepared by mixing IKB/S, carbon nanofibers (CNF, Sigma-Aldrich), and sodium carboxymethyl cellulose (CMC, Sigma-Aldrich)/Poly(styrene-co-butadiene) (SBR, Sigma-Aldrich) with water as a solvent and n-butanol (Sigma-Aldrich) as an additive to form a uniform slurry. The weight ratio of active material, CNF, and binder is 8:1:1. Then the slurry was single-sided and double-sided coated on a carbon-coated aluminium foil (Guangzhou Nano New Material Technology Co., Ltd). The S cathode was dried at 60°C under vacuum conditions for 12 hr and had a S areal loading of 4-6 mg cm⁻² per side. The cathode was calendered to 90% of its original thickness prior to use (10% calendering). It was punched to rectangular pieces (54 mm × 36 mm) for pouch cell use. The cathode porosity was calculated based on the density of element density of S and C; 2.1 g cm⁻³ was used as the cathode density with 0% porosity. The S electrode has a thickness of 140 μm at 6 mg cm⁻² S loading.

Assembly of pouch cell. Double-sided 50 μm Li foil (China Energy Lithium Co., Ltd.) was calendered onto a 9 μm Cu mesh (MTI Corp.) and punched to rectangular pieces (55.5 mm × 37.5 mm) as the Li anode of pouch cell. The separator for the pouch cell was Celgard 2400. Double-sided S cathode, separator, and double-sided Li anode were alternatively stacked together with two pieces of single-sided S cathode as the outer layer. The pouch cell was assembled in a dry room (0.1 RH%, 19 °C) of the Advanced Battery Facility Laboratory in PNNL. The electrolyte used in this study was 1 M lithium bis(trifluoromethanesulfonyl) imide (LiTFSI, Gotion) in 1,3-dioxolane (DOL, Gotion) and 1,2-dimethoxyethane (DME, Gotion) (1:1, v/v) with 0.3 M LiNO₃ (Sigma-Aldrich) as an additive. The electrolyte injection and pouch cell sealing were carried out in a glovebox filled with argon with both oxygen and moisture level below 1 ppm. The E/S ratio without further annotation means the applied E/S ratio that is the ratio of electrolyte volume (mL) to the sulfur mass (g) in the cell assembly. Pore-filling E/S ratio was estimated by the pore volume of cathode and separator divided by sulfur mass, which is 1.9 mL g⁻¹ in this paper (Supporting information).

Assembly of coin cell. The 2032-type (MTI Corp.) coin cell was assembled in the Ar-filled glovebox. The diameters of the cathode and anode were 12.7 mm and 15.9 mm, respectively. The fresh cathode was the single-sided IKB/S cathode. The fresh anode was 250 μm Li chips (MTI Corp.) for N/P 17 and single-sided 50 μm Li/Cu anode for N/P 1.4. The cycled electrode was punched from a double-sided electrode in the 313 Wh kg⁻¹ pouch cell after 22 cycles and tested directly without scraping the back side to avoid the physical damage. For the reassembled cell, the cycled electrode was assembled with fresh electrode and tested in coin cell with Celgard 2400 as the separator.

Electrochemical test

Before conducting the cell test, the pouch cell was sandwiched between two foam pads and fixed between two polyether ether ketone plates with four sets of screw/spring under an initial pressure of 20 psi. The electrochemical performance of the pouch cell was tested galvanostatically at 0.05 C in a voltage range of 1.7–2.8 V on an Arbin BT2000 at 25°C except for the first cycle at 0.02 C in a voltage range of 1.5–2.8 V. The charge/discharge specific capacity mentioned in this paper was calculated based on the S weight by excluding the carbon content. The electrochemical performance of the coin cell was tested galvanostatically on a LANHE battery tester CT2001A in a voltage range of 1.8–2.8 V at 30°C. The cumulative capacity is defined as the total discharge capacities delivered in the lifespan:

$$Cap_{cum} = 0.001 \sum_{i=1}^n Cap_i$$

where Cap_{cum} is the cumulative specific discharge capacity (Ah g⁻¹); Cap_i is the specific discharge capacity of the i cycle (mAh g⁻¹); n is the cycle number.

Post-mortem analysis of the cycled pouch cell

The cycled 313 Wh kg⁻¹ pouch cell was disassembled in an Ar-filled glovebox. Cycled electrodes of different regions were characterized and electrochemically tested in reassembled coin cell without washing treatment.

Characterization

Samples transferred to characterization instruments were sealed in air-proof containers filled with Ar to avoid air contamination. Observation of sample morphology was performed using a dual focused ion beam (FIB)/scanning electron microscope (SEM) (FEI Helios) system. X-ray photoelectron spectroscopy (XPS) was collected on a Physical Electronics Instruments Quantum 2000 scanning X-ray microprobe. X-ray fluorescence microscopy (XRF) and S K-edge X-ray absorption spectroscopy (XAS) experiments were carried out at the National Synchrotron Light Source (NSLS)-II TES Beamline (8-BM) at Brookhaven National Laboratory. A 7 × 7 mm² area was picked for different regions of R1, R2, and R3, with a spatial resolution of 25 μm.

Model description of electrolyte diffusion simulation in Li-S battery

One quarter of the battery was simulated given the symmetrical geometry features to speed up calculation. The simulation domain is depicted in Fig. S9 and consisted of one porous cathode (blue), one porous separator (yellow), and an active electrolyte (green) reservoir. The cut-view surfaces are set as symmetry and all other boundaries are non-flux, except the top surface of the separator (the bottom surface of the anode) where the electrolyte is consumed by chemical reaction. Under initial conditions, the micro pores of the cathode and separator, as well as the spare region, are filled with electrolyte. As the chemical reaction proceeds, the remaining electrolyte decreases gradually. The following assumptions were made in the modelling:

- The battery has a constant and uniform temperature distribution.
- Knudsen diffusion is neglected: Knudsen diffusion is important only when the mean free path of the molecule is similar to or larger than the pore diameter. Under the circumstance of this work, the electrolyte is a liquid that has mean free path at the magnitude of an angstrom, which is much smaller than the pore diameter of micrometer. Therefore, the Knudsen diffusion was neglected.
- Diffusion coefficient: The diffusion coefficient of this system is pretty complex. The effective diffusion coefficient depends on the chemical species and their concentrations, and the nano and microstructure of the cathode and separator. According to the literature results, a coefficient of 5 × 10⁻¹⁰ m² s⁻¹ was used.^{60, 61}
- The electrolyte was divided into two artificial components (A and B) with the same properties. Physically, they are still the same fluid. The initial mass fractions of components A and B are 0.001 and 0.999, respectively. Component B was assumed to be the active electrolyte that will be consumed and converted to A by the chemical reaction. This manipulation was made to facilitate the modelling.
- The reaction rate at the top surface of the separator is relative to the mass fraction of component B. The kinetic reaction rate in units of mg m⁻² h⁻¹ was estimated by:

$$R_k = \frac{R_a \rho \omega_B}{A}$$

where ρ , ω_B , and A are the density of the electrolyte, mass fraction of electrolyte B, and surface area of the separator, respectively. R_a is the apparent consuming rate of electrolyte, 1.96 × 10⁻⁴ mL h⁻¹, which was estimated by the electrolyte amount difference divided by cell life time difference by assuming that at the end of discharge, the electrolyte outside of electrode and separator pores was completely depleted.

Governing equations

Mass transfer in spare region:

$$\rho \frac{\partial \omega_j}{\partial t} - \rho D_j \nabla^2 \omega_j = 0$$

Mass transfer in cathode and separator:

$$\varepsilon \rho \frac{\partial \omega_j}{\partial t} - \rho D_{e,j} \nabla^2 \omega_j = 0$$

with:

ρ , electrolyte density, 1.13 × 10³ kg m⁻³

ε , porosity, sulfur cathode 66%, separator 45%

ω_j , mass fraction of component A or B

D_j , effective diffusion coefficient in spare volume, m² s⁻¹,

$$\text{defined as } \frac{1 - \omega_j}{\omega_j} D_B, 5 \times 10^{-10} \text{ m}^2 \text{ s}^{-1}$$

$D_{e,j}$, effective diffusion coefficient in cathode/separator, m^2

$$\frac{\varepsilon}{\tau} \frac{1 - \omega_j}{\omega_j} D_B$$

s^{-1} , defined as

To understand the effect of tortuosity on the electrolyte diffusion, two values of cathode tortuosity τ were selected. Considering the porous and nanostructures of sulfur host (IKB)

was used for our cathode,⁶² a high tortuosity of $1/\varepsilon^4$ (5.27) was used for electrode simulation (Fig. 5). To predict the electrolyte diffusion behavior in a low tortuosity electrode, a

low tortuosity value of $1/\varepsilon$ (1.52) was used for the simulation in Fig. S8.

The simulation was carried out using software COMSOL and a mesh independence study was performed to assure grid independence.

Conclusions

The failure mechanism of a realistic high-energy Li-S pouch cell has been studied and traced to material- and electrode-level understandings. A crucial prerequisite for delivering a high-energy Li-S battery is the simultaneous integration of a reasonably loaded S cathode, a lean amount of electrolyte, and a limited Li anode. These components interrelate with each other in the high-energy pouch cell and have significant effects on cell cycle life, which is drastically different than coin cell configurations. Under realistic conditions, the cycle life of the Li-S pouch cell deteriorates rapidly because both the electrolyte consumption and the reaction heterogeneity. The uneven reaction in different locations of the same cathode/anode layer has been captured and assigned to the hindered electrolyte redistribution through the nanosized electrode pores upon the cycling. The fluid-flow simulation results indicate that electrolyte depletion originates from the center of the cathode and spreads to the edges. Instead of electrolyte difference occurring in the electrode perpendicular direction, the slow electrolyte diffusion along the large-size and porous cathode plane is a rate-limiting step. Accordingly, electrochemical reactions are gradually “shut off” starting from the center of the cathode. Rather than polysulfide dissolution/shuttling or Li anode limiting, electrolyte drying up and heterogeneous distribution are believed to act as the dominant reasons for the early cell termination in Li-S pouch cells with both the high S loading cathode and extremely low E/S ratio. Potential strategies that could help extend the cell lifespan should be built upon comprehensive consideration of material properties, electrode architecture, electrolyte selection, and cell design. A full spectrum understanding of the dynamic interactions of key cell components will be critical to unlock the full potential of Li-S battery technologies.

Author Contributions

D. P. L., J. X., J. L. designed research; L. S., S.M.B., Z. S., C.W., C. N., P.N., H. L., A. Y. B., C. S. A., J. Q., S.F., X. R., D. Y. L., X. Q. Y., F.G.

performed research; D.P.L., J. X., J. L., L. S., S.M.B., and C.W. analysed data; and L. S., D.P.L. J. X., J. L. wrote the paper.

Conflicts of interest

There are no conflicts to declare.

Acknowledgements

This research was supported by the Assistant Secretary for Energy Efficiency and Renewable Energy, Office of Vehicle Technologies of the U.S. Department of Energy through the Advanced Battery Materials Research (BMR) Program (Battery500Consortium and BMR under Contract No. DEAC02-05CH11231 and DEAC02-98CH10886). PNNL is operated by Battelle under Contract No. DE-AC05-76RL01830 for the U.S. Department of Energy. The National Synchrotron Light Source II, a User Facility at Brookhaven National Laboratory, is supported by the U.S. Department of Energy Office of Science under Contract No. DE-SC0012704.

Notes and references

1. J. Xiao, *Adv. Energy Mater.*, 2015, **5**.
2. Y. L. Cao, M. Li, J. Lu, J. Liu and K. Amine, *Nature Nanotechnology*, 2019, **14**, 200-207.
3. Y. V. Mikhaylik and J. R. Akridge, *J. Electrochem. Soc.*, 2004, **151**, A1969-A1976.
4. J. Shim, K. A. Striebel and E. J. Cairns, *J. Electrochem. Soc.*, 2002, **149**, A1321-A1325.
5. X. L. Ji, K. T. Lee and L. F. Nazar, *Nat. Mater.*, 2009, **8**, 500-506.
6. L. F. Xiao, Y. L. Cao, J. Xiao, B. Schwenzer, M. H. Engelhard, L. V. Saraf, Z. M. Nie, G. J. Exarhos and J. Liu, *Adv. Mater.*, 2012, **24**, 1176-1181.
7. Z. W. Seh, W. Y. Li, J. J. Cha, G. Y. Zheng, Y. Yang, M. T. McDowell, P. C. Hsu and Y. Cui, *Nat. Commun.*, 2013, **4**.
8. M. P. Yu, A. J. Wang, F. Y. Tian, H. Q. Song, Y. S. Wang, C. Li, J. D. Hong and G. Q. Shi, *Nanoscale*, 2015, **7**, 5292-5298.
9. D. P. Lv, J. M. Zheng, Q. Y. Li, X. Xie, S. Ferrara, Z. M. Nie, L. B. Mehdi, N. D. Browning, J. G. Zhang, G. L. Graff, J. Liu and J. Xiao, *Adv. Energy Mater.*, 2015, **5**, 8.
10. Y. V. Mikhaylik, I. Kovalev, R. Schock, K. Kumaresan, J. Xu and J. Affinito, *ECS Trans.*, 2010, **25**, 23-34.
11. Y. S. Su and A. Manthiram, *Chemical Communications*, 2012, **48**, 8817-8819.
12. D. Aurbach, E. Pollak, R. Elazari, G. Salitra, C. S. Kelley and J. Affinito, *J. Electrochem. Soc.*, 2009, **156**, A694-A702.
13. A. Rosenman, R. Elazari, G. Salitra, E. Markevich, D. Aurbach and A. Garsuch, *J. Electrochem. Soc.*, 2015, **162**, A470-A473.
14. L. M. Suo, Y. S. Hu, H. Li, M. Armand and L. Q. Chen, *Nat. Commun.*, 2013, **4**, 9.
15. C. Weller, S. Thieme, P. Hartel, H. Althues and S. Kaskel, *J. Electrochem. Soc.*, 2017, **164**, A3766-A3771.
16. L. Qie, C. X. Zu and A. Manthiram, *Adv. Energy Mater.*, 2016, **6**.

17. Y. W. Ma, H. Z. Zhang, B. S. Wu, M. R. Wang, X. F. Li and H. M. Zhang, *Sci. Rep.*, 2015, **5**, 10.
18. X.-B. Cheng, C. Yan, J.-Q. Huang, P. Li, L. Zhu, L. Zhao, Y. Zhang, W. Zhu, S.-T. Yang and Q. Zhang, *Energy Storage Materials*, 2017, **6**, 18-25.
19. Y. S. Ye, F. Wu, Y. T. Liu, T. Zhao, J. Qian, Y. Xing, W. L. Li, J. Q. Huang, L. Li, Q. M. Huang, X. D. Bai and R. J. Chen, *Adv. Mater.*, 2017, **29**.
20. X. Q. Yu, H. L. Pan, Y. N. Zhou, P. Northrup, J. Xiao, S. Bak, M. Z. Liu, K. W. Nam, D. Y. Qu, J. Liu, T. P. Wu and X. Q. Yang, *Adv. Energy Mater.*, 2015, **5**.
21. C. Barchasz, J. C. Lepretre, F. Alloin and S. Patoux, *J. Power Sources*, 2012, **199**, 322-330.
22. C. X. Zu, Y. Z. Fu and A. Manthiram, *J. Mater. Chem. A*, 2013, **1**, 10362-10367.
23. A. Krause, S. Dorfler, M. Piwko, F. M. Wisser, T. Jaumann, E. Ahrens, L. Giebeler, H. Althues, S. Schadlich, J. Grothe, A. Jeffery, M. Grube, J. Bruckner, J. Martin, J. Eckert, S. Kaskel, T. Mikolajick and W. M. Weber, *Sci. Rep.*, 2016, **6**.
24. H. Schneider, T. Weiss, C. Scordilis-Kelley, J. Maeyer, K. Leitner, H. J. Peng, R. Schmidt and J. Tomforde, *Electrochim. Acta*, 2017, **243**, 26-32.
25. J. Liu, Z. N. Bao, Y. Cui, E. J. Dufek, J. B. Goodenough, P. Khalifah, Q. Y. Li, B. Y. Liaw, P. Liu, A. Manthiram, Y. S. Meng, V. R. Subramanian, M. F. Toney, V. V. Viswanathan, M. S. Whittingham, J. Xiao, W. Xu, J. H. Yang, X. Q. Yang and J. G. Zhang, *Nat. Energy*, 2019, **4**, 180-186.
26. J. Xiao, Y. Yang, D. Liu and Z. D. Deng, Machine learning-assisted lithium metal battery design software, <https://www.pnnl.gov/technology/li-batt-design-app>, (accessed Pacific Northwest National Laboratory, June 28, 2020).
27. C. Barchasz, J. C. Lepretre, S. Patoux and F. Alloin, *Electrochim. Acta*, 2013, **89**, 737-743.
28. S. S. Zhang, *Electrochim. Acta*, 2012, **70**, 344-348.
29. S. S. Zhang and J. A. Read, *J. Power Sources*, 2012, **200**, 77-82.
30. C. X. Zu, L. J. Li, J. H. Guo, S. F. Wang, D. L. Fan and A. Manthiram, *J. Phys. Chem. Lett.*, 2016, **7**, 1392-1399.
31. D. P. Lu, Q. Y. Li, J. Liu, J. M. Zheng, Y. X. Wang, S. Ferrara, J. Xiao, J. G. Zhang and J. Liu, *Acs Applied Materials & Interfaces*, 2018, **10**, 23094-23102.
32. P. Northrup, *Journal of Synchrotron Radiation*, 2019, **26**, 2064-2074.
33. I. J. Pickering, G. N. George, E. Y. Yu, D. C. Brune, C. Tuschak, J. Overmann, J. T. Beatty and R. C. Prince, *Biochemistry*, 2001, **40**, 8138-8145.
34. A. Manceau and K. L. Nagy, *Geochim. Cosmochim. Acta*, 2012, **99**, 206-223.
35. M. U. M. Patel, I. Arcon, G. Aquilanti, L. Stievano, G. Mali and R. Dominko, *Chemphyschem*, 2014, **15**, 894-904.
36. Y. Diao, K. Xie, S. Z. Xiong and X. B. Hong, *J. Electrochem. Soc.*, 2012, **159**, A1816-A1821.
37. D. Aurbach, M. L. Daroux, P. W. Faguy and E. Yeager, *J. Electrochem. Soc.*, 1988, **135**, 1863-1871.
38. X. Chen, T.-Z. Hou, B. Li, C. Yan, L. Zhu, C. Guan, X.-B. Cheng, H.-J. Peng, J.-Q. Huang and Q. Zhang, *Energy Storage Materials*, 2017, **8**, 194-201.
39. C. Fiedler, B. Luerssen, M. Rohnke, J. Sann and J. Janek, *J. Electrochem. Soc.*, 2017, **164**, A3742-A3749.
40. W. Xu, J. L. Wang, F. Ding, X. L. Chen, E. Nasybutin, Y. H. Zhang and J. G. Zhang, *Energy Environ. Sci.*, 2014, **7**, 513-537.
41. W. K. Lewis, *Industrial & Engineering Chemistry*, 1921, **13**, 427-432.
42. T. Sherwood, *Industrial & Engineering Chemistry*, 1932, **24**, 307-310.
43. Q. Zhao, X. F. Hu, K. Zhang, N. Zhang, Y. X. Hu and J. Chen, *Nano Letters*, 2015, **15**, 721-726.
44. H. B. Lin, L. Q. Yang, X. Jiang, G. C. Li, T. R. Zhang, Q. F. Yao, G. W. Zheng and J. Y. Lee, *Energy Environ. Sci.*, 2017, **10**, 1476-1486.
45. H. L. Pan, K. S. Han, M. H. Engelhard, R. G. Cao, J. Z. Chen, J. G. Zhang, K. T. Mueller, Y. Y. Shao and J. Liu, *Advanced Functional Materials*, 2018, **28**.
46. H. L. Pan, J. Z. Chen, R. G. Cao, V. Murugesan, N. N. Rajput, K. S. Han, K. Persson, L. Estevez, M. H. Engelhard, J. G. Zhang, K. T. Mueller, Y. Cui, Y. Y. Shao and J. Liu, *Nat. Energy*, 2017, **2**.
47. L. S. Li, R. M. Erb, J. J. Wang, J. Wang and Y. M. Chiang, *Adv. Energy Mater.*, 2019, **9**.
48. W. Pfleging, *Nanophotonics*, 2018, **7**, 549-573.
49. L. Chen, Z. N. Huang, R. Shahbazian-Yassar, J. A. Libera, K. C. Klavetter, K. R. Zavadil and J. W. Elam, *Acs Applied Materials & Interfaces*, 2018, **10**, 7043-7051.
50. R. G. Cao, J. Z. Chen, K. S. Han, W. Xu, D. H. Mei, P. Bhattacharya, M. H. Engelhard, K. T. Mueller, J. Liu and J. G. Zhang, *Advanced Functional Materials*, 2016, **26**, 3059-3066.
51. K. Dokko, N. Tachikawa, K. Yamauchi, M. Tsuchiya, A. Yamazaki, E. Takashima, J. W. Park, K. Ueno, S. Seki, N. Serizawa and M. Watanabe, *J. Electrochem. Soc.*, 2013, **160**, A1304-A1310.
52. C. W. Lee, Q. Pang, S. Ha, L. Cheng, S. D. Han, K. R. Zavadil, K. G. Gallagher, L. F. Nazar and M. Balasubramanian, *Acs Central Science*, 2017, **3**, 605-613.
53. S. R. Chen, J. M. Zheng, D. H. Mei, K. S. Han, M. H. Engelhard, W. G. Zhao, W. Xu, J. Liu and J. G. Zhang, *Adv. Mater.*, 2018, **30**.
54. S. H. Jiao, X. D. Ren, R. G. Cao, M. H. Engelhard, Y. Z. Liu, D. H. Hu, D. H. Mei, J. M. Zheng, W. G. Zhao, Q. Y. Li, N. Liu, B. D. Adams, C. Ma, J. Liu, J. G. Zhang and W. Xu, *Nat. Energy*, 2018, **3**, 739-746.
55. Z. Li, S. G. Zhang, S. Terada, X. F. Ma, K. Ikeda, Y. Kamei, C. Zhang, K. Dokko and M. Watanabe, *Acs Applied Materials & Interfaces*, 2016, **8**, 16053-16062.
56. K. Fu, Y. H. Gong, G. T. Hitz, D. W. McOwen, Y. J. Li, S. M. Xu, Y. Wen, L. Zhang, C. W. Wang, G. Pastel, J. Q. Dai, B. Y. Liu, H. Xie, Y. G. Yao, E. D. Wachsman and L. B. Hu, *Energy Environ. Sci.*, 2017, **10**, 1568-1575.
57. X. A. Liang, Z. Y. Wen, Y. Liu, H. Zhang, L. Z. Huang and J. Jin, *J. Power Sources*, 2011, **196**, 3655-3658.
58. X. Y. Tao, Y. Y. Liu, W. Liu, G. M. Zhou, J. Zhao, D. C. Lin, C. X. Zu, O. Sheng, W. K. Zhang, H. W. Lee and Y. Cui, *Nano Letters*, 2017, **17**, 2967-2972.
59. X. Y. Yao, N. Huang, F. D. Han, Q. Zhang, H. L. Wan, J. P. Mwiszerwa, C. S. Wang and X. X. Xu, *Adv. Energy Mater.*, 2017, **7**.
60. A. Ehrl, J. Landesfeind, W. A. Wall and H. A. Gasteiger, *J. Electrochem. Soc.*, 2017, **164**, A826-A836.
61. M. Safari, C. Y. Kwok and L. F. Nazar, *ACS central science*, 2016, **2**, 560-568.

Journal Name

ARTICLE

62. S. Malifarge, B. Delobel and C. Delacourt, *J. Electrochem. Soc.*, 2017, **164**, E3329-E3334.